Progress In Electromagnetics Research, Vol. 141, 517–535, 2013

AN ACCURATE IMAGING ALGORITHM FOR MILLIMETER WAVE SYNTHETIC APERTURE IMAGING RADIOMETER IN NEAR-FIELD

Jianfei Chen[1], Yuehua Li[1, *], Jianqiao Wang[1], Yuanjiang Li[1, 2], and Yilong Zhang[1]

[1]School of Electronic Engineering and Optoelectronic Technology, Nanjing University of Science and Technology, Nanjing 210094, China

[2]Institute of Electronic and Information, Jiangsu University of Science and Technology, Zhenjiang 212000, China

Abstract—Due to the fact that the imaging distance is similar to the dimension of synthetic aperture antenna in near-field, the Fourier imaging theory used in the traditional synthetic aperture imaging radiometer (SAIR), which is based on the far-field approximation, is invalid for near-field synthetic aperture imaging. This paper is devoted to establishing an accurate imaging algorithm for near-field millimeter wave SAIR. Firstly, the near-field synthetic aperture imaging theory is deduced and its relationship to the far-field imaging theory analyzed. Then, an accurate imaging algorithm based on the near-field imaging theory is established. In this method, the quadratic phase item and antenna pattern are taken into consideration, and the image reconstruction is performed by minimizing the Total-Variation norm of brightness temperature image, which reduces the influence of the visibility observation error and improves imaging precision. Finally, the effectiveness of the proposed imaging algorithm has been tested by means of several simulation experiments, and the superiority is also demonstrated by the comparison between it and the existing Fourier transform methods. The results demonstrate that the proposed method is an efficient, feasible imaging algorithm for near-field millimeter wave SAIR.

Received 7 June 2013, Accepted 20 July 2013, Scheduled 1 August 2013

* Corresponding author: Yuehua Li (hmb4507@mail.njust.edu.cn).

1. INTRODUCTION

Millimeter-wave imaging radiometers are powerful sensors for high-resolution observations of personal security. Unlike microwave imaging, millimeter-wave imaging has shorter wavelengths, which is significant to obtaining the image with better spatial resolution. Compared to optical and infrared radiation, it can "see through" obscuring materials such as clothing, cardboard, plastics, and wood with comparatively trifling loss. Different from familiar X-ray imaging, millimeter-wave imaging is commonly regarded as harmless to humans [1–3]. However, due to the tradeoff between antenna aperture and spatial resolution, traditional millimeter-wave imaging system cannot achieve the desired high spatial resolution.

Interferometric aperture synthesis imaging technology, initially developed for radio astronomy in the 1980s [4, 5], can well solve the contradiction between the antenna aperture and spatial resolution. Its basic idea is to use a thin array composed of small aperture antennas to achieve a large aperture antenna by performing correlation operations in pairs. Each complex correlation is a sample of the visibility function which, in the ideal case, is the spatial Fourier transform of the brightness temperature distribution [6]. Then the Millimeter-wave image can be reconstructed by some imaging algorithm from the visibility function. Therefore, the interferometric aperture synthesis imaging technology has attracted more and more attention and obtained great progress in the past ten years. After series of land-based and airborne synthesis aperture imaging systems were built [7, 8], the satellite-based SAIR using aperture synthesis in both directions (named SMOS/MIRAS) developed by the European space agency (ESA) was also launched in 2009, and successfully passed the track debugging and test operating phase [9–11]. It is an important symbol for the SAIR to enter the stage of practical application as a replacement of the traditional real aperture imaging radiometer.

On the other hand, high spatial resolution is also the most desired requirement for near-field imaging applications, such as security detection of concealed weapons or other contrabands, all weather reconnaissance and surveillance, and ground penetrating imaging for landmine detection or archeology. As a cost-effective technique with high imaging resolution, aperture synthesis imaging would be extensively used in near-field applications. However, due to the fact that the traditional Fourier imaging theories are based on the far-field approximation, they are not suitable for near-field synthetic aperture imaging, and the near-field curvature effect must be taken into account when the target is in the near-field of the antenna array.

Now the imaging method for near-field SAIR is a problem to be solved, and some solutions have been proposed in [12–15]. They can be classified into two types. One is based on hardware transformation. The antenna array is physically rearranged from planar distribution to circular or spherical distribution. This curved array should fit the curvature of the incident spherical wave, so that the relation between the incident wave and measured visibility is still Fourier transform [16, 17]. But this method is only suitable for the targets within a tiny area and fixed on the focus point of the spherical array, so it does not fit for practical application. The other one is based on software modification. It still employs the traditional planar array but theoretically modifies the measured visibility by adding a correction phase term to get the equivalent far-field visibility, which is also the modified Fourier method [18, 19]. Nevertheless, this kind of method is directly to use Fourier inversion algorithm for solving the approximate brightness temperature distribution, and ignores the visibility observation error caused by the antenna position errors, and partial coherence between the radiation sources and some other factors. So the images reconstructed by this method still have obvious blur and noise pollution in practical application. In this paper, we first deduce the synthetic aperture imaging theory in near-field case, and analyze the difference between it and the far-field synthetic aperture imaging theory. Then, an accurate imaging method based on this near-field synthetic aperture imaging theory is proposed. In this method, the quadratic phase item and antenna pattern are taken into consideration, and the image reconstruction is performed by minimizing the Total-Variation norm of brightness temperature image, which reduces the influence of partial coherence and improves the imaging precision. The effectiveness of this proposed imaging algorithm has been tested by means of several simulation experiments, and the superiority is also demonstrated by comparing with the existing Fourier transform methods. The simulation results demonstrate that the proposed method is an efficient, feasible imaging algorithm for near-field millimeter-wave SAIR.

2. THE NEAR-FIELD SYNTHETIC APERTURE IMAGING THEORY

Due to the shorter imaging distance of the near-field imaging, the far-field imaging method based on the far-field approximation is not suitable for near-field SAIR. Here, a brief analysis of near-field synthetic aperture imaging model based on "T" antenna array is demonstrated. As shown in Fig. 1, an extended radiation source S is

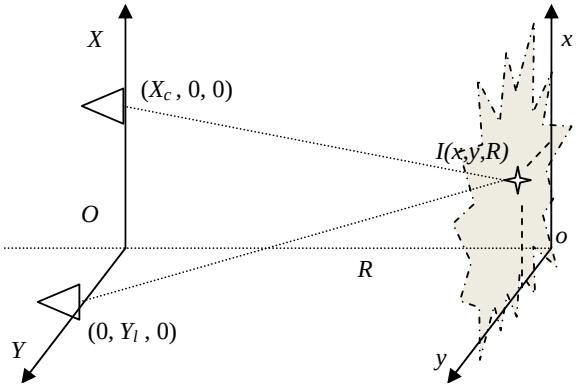

Figure 1. Geometry diagram of near-field synthetic aperture imaging.

located on plane oxy, with its radiation electromagnetic wave frequency ω and wavelength λ, and the antenna array is located on plane OXY.

The radiation source S is dispersed into M small parts, the distance between the radiation source S_i and the two antennas is R_i^c and R_i^l. According to [19], the visibility samples for any two antennas labeled c and l, can be expressed as

$$\begin{aligned} V_{c,l} &= \left\langle E_c\left(R_i^c, t\right) \cdot E_l^*\left(R_i^l, t\right)\right\rangle \\ &= \sum_{i=0}^{M} T_i(x,y) F_i^c(x,y) F_i^l(x,y)^* r_{c,l} \exp\left[-jk\left(R_i^c - R_i^l\right)\right] \end{aligned} \quad (1)$$

where, $\langle\cdot\rangle$ denotes time integration operation, (x, y) the coordinate of the radiation source S_i, $T(x, y)$ the normalized brightness temperature, and $r_{c,l}$ the so called fringe-wash function [20], which accounts for spatial decorrelation effects. In the limiting narrow-band imaging system, the decorrelation effects are negligible and $r_{c,l} = 1$, $\exp[-jk(R_i^c - R_i^l)]$ denotes phase difference of two antenna, which is the key factor for the synthetic aperture imaging. According to Fig. 1, the distance R_i^c and R_i^l through the Taylor expansion approximation can be expressed as

$$R_i^c = \sqrt{(x - X_c)^2 + y^2 + R^2} \approx R + \frac{(x - X_c)^2 + y^2}{2R} \quad (2)$$

$$R_i^l \approx R + \frac{x^2 + (y - Y_l)^2}{2R} \quad (3)$$

Combined with the two equations (Eqs. (4), (5)), $k\Delta R$ can be rewritten

as

$$k\Delta R = k\left(R_i^c - R_i^l\right) = k\left(-xX_c + yY_l\right)/R + k\left(X_c^2 - Y_l^2\right)/2R \quad (4)$$

Then define spatial frequency domain variable as: $v = -kX_c/R$, $h = kY_l/R$, $\varphi(v,h) = k(X_c^2 - Y_l^2)/2R$. So

$$k\Delta R = k\left(R_i^c - R_i^l\right) = vx + hy + \varphi(v,h) \quad (5)$$

Substituting Eq. (5) into Eq. (1), then rewriting it as the integral form, we can get the near-field synthetic aperture imaging formula as follows

$$V(v,h) = e^{-\varphi(v,h)} \iint\limits_{xoy} T(x,y) F^c(x,y) F^l(x,y)^* \exp[-jk(vx+hy)]dxdy \quad (6)$$

where $\varphi(v,h)$ is the quadratic phase-modified item, $V(v,h)$ the visibility function measured by the imaging system in plane OXY, and $T(x,y)$ the brightness temperature distribution.

Generally, the field of view (FOV) is concentrated in the center of system beam, so the two antenna patterns can be ignored ($T^\circ(x,y) \approx T(x,y)$). And the imaging formula can be rewritten as

$$V(v,h) = e^{-\varphi(v,h)} \iint\limits_{xoy} T^\circ(x,y) \exp[-jk(vx+hy)]dxdy \quad (7)$$

As Eq. (7) shows, the visibility function (V) of the antenna pairs is equal to the product of the quadratic phase-modified item ($e^{-\varphi(v,h)}$) and the inverse Fourier transformation of brightness temperature distribution (T). Introducing the 2-d Fourier transform symbols (IFT_2 and FT_2) to Eq. (7), it can be rewritten as

$$V(v,h) = \exp(-j\varphi)\mathrm{IFT}_2\left[T^\circ(x,y)\right] \quad (8)$$

Therefore the solving equation of brightness temperature distribution is expressed as:

$$T^\circ(x,y) = \mathrm{FT}_2[\exp(j\varphi)V(v,h)] \quad (9)$$

This is the modified Fourier imaging algorithm for near-field millimeter SAIR. Compared with far-field direct Fourier imaging theory, due to the effect of near-field spherical wave, near-field synthetic aperture imaging has a phase-modified item ($e^{-\varphi(v,h)}$), which is the key for the near-field imaging. It can be seen as a convex lens with the focal length R, which makes the near-field spherical wave became plane wave. In far-field imaging case, the imaging distance $R \gg D_{SA}$ and $\varphi(v,h) \approx 0$, so the phase-modified item is ignored in direct Fourier imaging theory. But it can't be ignored for near-field imaging,

otherwise the point spread function (PSF) of the near-field SAIR will be widened, as a result the acquired image will also become fuzzy. The closer the imaging distance is, the more indistinct the image is. The influence of quadratic phase-modified item on the near field SAIR is illustrated in Fig. 2. The main parameters of these four simulations are as follows. The imaging distance is 10 m, the frequency is 37 GHz, the wavelength is about 8 mm, the antenna array is 100×100 and the array size is $1\,\text{m} \times 1\,\text{m}$. The detailed simulation model will be demonstrated in Section 4.

Due to the fact that the phase-modified item is ignored in direct Fourier imaging theory, in other word, an incorrect imaging distance

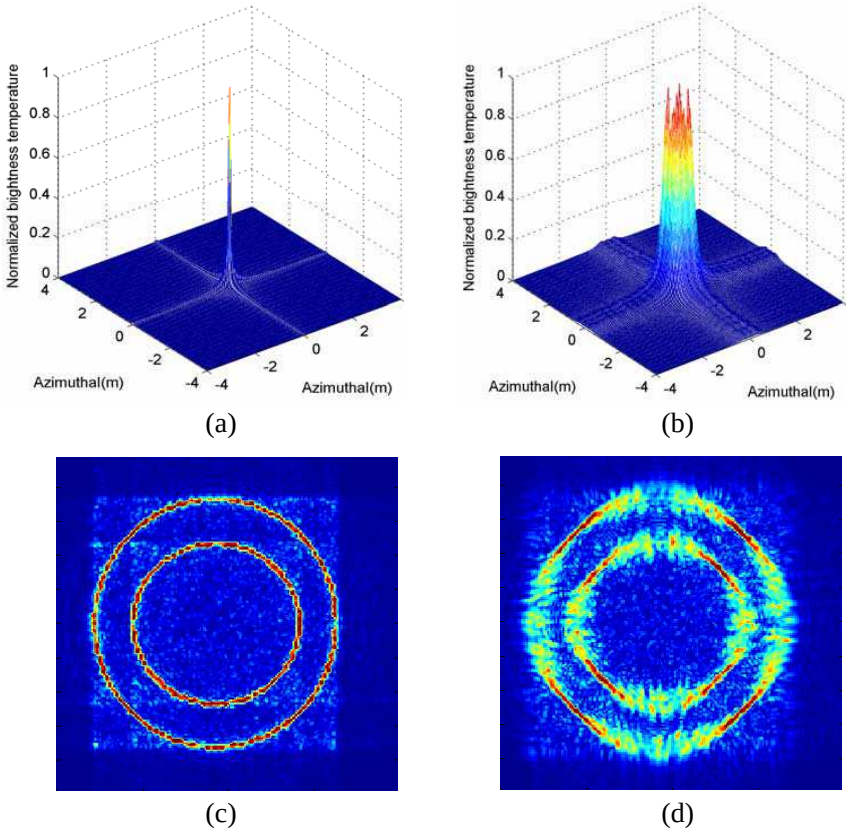

Figure 2. The influence of quadratic phase-modified item on near-field SAIR (the imaging distance is 10 m). (a) PSF of modified Fourier method. (b) PSF of direct Fourier method. (c) Imaging result of modified Fourier method. (d) Imaging result of direct Fourier method.

R_{ic} is used to replace the correct distance R in $\varphi(v, h)$. The PSF of the direct Fourier imaging algorithm is more widened than the modified Fourier imaging algorithm with the correct imaging distance, as shown in Figs. 2(a)–(b). And a simulation experiment of the simple scene with two concentric circles is made here. Due to the fact that the phase-modified item with correct distance R is used in modified Fourier method, its imaging result (Fig. 2(c)) is clearer than the result (Fig. 2(d)) of direct Fourier method with widened PSF. But these two Fourier imaging methods are all devoted to solve the approximate brightness temperature distribution (T°). They ignore the influence of partial coherence between the targets and the visibility observation error caused by the error of detection system, etc.. So their imaging results have some errors, which reduce the visibility of the reconstructed image. It is also demonstrated by the imaging results shown in Fig. 2, there are some dim irregular brightness spots near the two concentric circles.

3. DESCRIPTION OF THE PROPOSED ACCURATE IMAGING ALGORITHM

According to the analysis in the second section, we conclude that the imaging effect can be improved by the modified Fourier imaging method with the quadratic phase item. But the partial coherence between the radiation sources and the visibility observation error are inevitable in actual imaging conditions, its improvement is obtained obviously only when the object is simple to be identified (radiation source distribution is regular and sparse), as shown in Fig. 2. However, it is hard to get an accurate image in the actual detection conditions when the radiation source distribution is irregular and not sparse. These are verified by simulation results shown in Figs. 6–9, due to the high radiation intensity of the upper wing, the partial coherence value between it and other weak radiation source is too high, as a result there has serious noise pollution near the upper wing. As shown in Figs. 6–9(b), even the images are carried on the simple filtering operation (Wiener filtering or median filtering), many low light noise pollution still exist near the target, which bring the difficulties of determining target outline and affect the visibility of image seriously. We know that these influences can be reduced by increasing the integration time of the received signal. But this will increase the imaging time, affect the application of the SAIR in the real-time imaging seriously. This paper devotes to establish an accurate imaging algorithm to reduce these impacts. For more accurately describing the near field synthetic aperture imaging, we rewrite the near field imaging formula as the

below matrix equation

$$\mathbf{V_{C\times L}} = \mathbf{D1_{C\times M}T_{M\times N}D2_{N\times L}} + \mathbf{\Delta V_{C\times L}} \tag{10}$$

where, $\mathbf{V}$ is the measured near-field visibilities matrix, $\mathbf{T}$ the brightness temperature matrix, $\Delta\mathbf{V}$ the visibility observation error, and $\mathbf{D1}$ and $\mathbf{D2}$ are the coefficient matrixes, which characterize the system configuration and target spatial distribution, the elements of $\mathbf{D1}$ and $\mathbf{D2}$ are

$$d1_{c,m} = f^c\left(x_m - X_c\right) f^l(x_m) \exp\left[-jk\left(X_c^2/2R - x_m X_c/R\right)\right] \tag{11}$$

$$d2_{n,l} = f^c(y_n) f^l(y_n - Y_l) \exp\left[-jk\left(Y_l^2/2R - y_n Y_l/R\right)\right] \tag{12}$$

where, x_m and y_n are the coordinates of radiation source S_i, and the corresponding bright temperature value is $T(m,n)$.

X_c and Y_l are the ordinate and abscissa of the antennas, respectively, the corresponding visibility value is $V(c,l)$. For the "T" antenna array, $Y_c = 0$ and $X_l = 0$.

$f^{\#}(\cdot)$ is the 1-d antenna pattern. For convenient analysis, we assume that all the antennas have the same antenna pattern in this paper. Generally, the FOV of the imaging system is concentrated in the center of system antenna beam. We use the one-dimensional antenna pattern to approximately replace the two-dimensional antenna pattern as

$$F^{\#}(x,y) = f^{\#}(x) f^{\#}(y) \tag{13}$$

In actual millimeter wave SAIR, due to the limit of antenna array, the dimension of the visibility function (V) is significantly less than the brightness temperature matrix (T). So the matrix equation (Eq. (10)) is an underdetermined equation, and the visibility observation error ΔV exists in the imaging process. Under this circumstance, the most effective method is to use the regularization method to solve this problem. In regularization method, the characteristic information about the real solutions is attached to the solution set and the additional information is used to restrain the solving process. The regularization solution model of Eq. (10) can be expressed as

$$\min_T J(T) = ||D1 \times T \times D2 - V||_F^2 + \mu\Psi(T) \tag{14}$$

where, $||D1 \times T \times D2 - V||_F^2$ is the fidelity term, which guarantees the difference between actual visibility function and the observation visibility function is small enough, $\Psi(T)$ the regularization item, also named as the constraint condition item, and μ the regularization parameter, which is used to balance the fidelity term and regularization term. Usually, we choose μ to be small enough in order not to degrade the spatial resolution significantly.

The charm of regularization method lies in seeking an approximate solution with the actual physical meaning, and ensuring that the approximate solution has strong stability. In this method, the prior information of the actual image is attached to the millimeter image reconstruction as the regularization item, which not only makes the ill-conditioned problem becoming a well-conditioned problem, but also makes the recovery image more close to the real source image. Therefore, the key of the regularization is how to use prior knowledge to structure the regularization term. Some existing study shows that if the total-variation (TV) function is chosen as the regularization term the image reconstruction can obtain a satisfactory effect [21, 22]. It is widely used in several applications such as image denoising, deblurring and MRI image recovery, mainly due to its desirable properties such as convexity, ability to preserve edges, as well as invariance to image shifts and rotations. For an image of T, its discrete isotropic TV norm is defined as

$$\mathrm{TV}(T) = \sum_{i,j \in T} \left\{ \begin{array}{l} |T(i+1,j) - T(i,j)| \\ +|T(i,j+1) - T(i,j)| \end{array} \right\} \tag{15}$$

And Eq. (14) can be reformulated as

$$\min_T J(T) = ||D1 \times T \times D2 - V||_F^2 + \mu \mathrm{TV}(T) \tag{16}$$

Now the reconstruction problem becomes a typical problem of solving the convex function optimization. There are numerous state-of-the-art optimization methods designed to solve it [23–26]. In this paper, we use the fast proximal-gradient projection algorithm (FGP) proposed in [26] to solve this convex function optimization problem. It is a fast and robust method that solves minimum l_1 problems and a large number of extensions including TV minimization with the accelerated convergence rate of $O(k^{-2})$. The key of this accurate imaging algorithm is calculating the coefficient matrixes $D1$ and $D2$, which means to calculate every element in the matrix according to Eqs. (11) and (12). In these formulae, the distance R can be modified. It can be considered as a focusing operation in the imaging process. Therefore, the clarity of the image can be improved by changing distance R in the process of actual millimeter image reconstruction.

4. SIMULATION AND RESULTS

4.1. Simulation Model

The numerical simulation is helpful for evaluating the performance of the proposed imaging algorithm. Here a simulation model with a

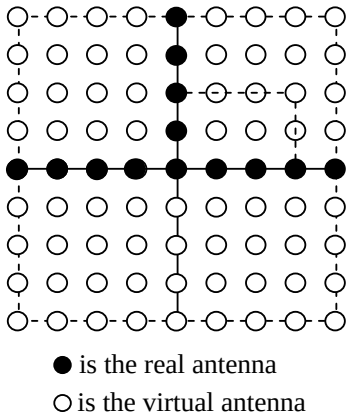

Figure 3. Diagram of "T" antenna array.

40×40 "T" antenna array is established (see Fig. 3). In this simulation model, the real antennas (solid round) are placed on the axis to constitute a "T" type array, and the corresponding visibility values are generated by the cross-correlation of these antennas with the original antenna. In the relative, the visibility values conforming to the virtual antennas are obtained by the cross-correlation of the real antennas located at the corresponding X and Y. So the visibility function of the upper plane can be calculated by this method. The remaining visibility function is obtained by the symmetric conjugate of the visibility function. The antenna elements are small horn antennas with large beam pattern, which are especially suitable for millimeter wave SAIR. And the distance between antennas is about 1.25λ ($\lambda = 8\,\text{mm}$).

In the process of simulation, for simulating the actual synthetic aperture imaging accurately, we assume that each discrete target has the ability of radiating millimeter wave. Its radiation intensity is the corresponding brightness temperature, and its phase shift is unique. The received signal of each antenna is obtained by the integral operation of the radiation waves generated by the discrete sources, and the visibility samples are calculated by the cross-correlated calculation of each antenna pairs. Then the Fourier imaging methods and the proposed accurate imaging method are used to reconstruct the millimeter images. Parameter μ in Eq. (16) is set to be 0.2. For the purpose of comparing the imaging effects of these imaging methods in far-field and near-field case, simulation experiments under the far-field and near-field condition are performed respectively in this paper. For

the SAIR, the far-field condition is usually defined as [15]

$$\begin{cases} R_{f1} \geq 2D_{SA}^2/\lambda & \text{general far-field,} \\ R_{f2} \geq 20D_{SA}^2/\lambda & \text{absolute far-field,} \end{cases} \tag{17}$$

where, D_{SA} is the array size of SAIR. According to this criterion, the general far-field of this simulation model is 40 m, and the absolute far-field is 400 m. The simulations are performed in four situations, as shown in Table 1.

Table 1. Distance settings in imaging simulations.

	Extreme near-field	General near-field	General far-field	Absolute far-field
Criterion	$R < 0.1R_{f1}$	$0.1R_{f1} \leq R < R_{f2}$	$R_{f1} \leq R < R_{f2}$	$R \geq R_{f2}$
Distance	1 m	10 m	60 m	400 m

4.2. One-dimensional Simulation Experiments

Here, a series of simulation experiments with 1-d extended source is performed to validate the effectiveness of the proposed method. As Fig. 4 shows, the simulation target consists of three parts: the right section is an ideal triangle wave, the middle section is the 1-d truncation drawn from an actual gray image, and the left section is an ideal rectangular wave. The Fourier methods are tested for comparison. The simulation results are shown in Fig. 4, and the imaging distances are set as Table 1.

In order to compare the results of these imaging methods objectively, their root-mean square errors (RMSEs) are calculated as the follow formula

$$\text{RMSE}(X', X_o) = \sqrt{\sum_i [X'(i) - X_o(i)]^2} \Big/ \sqrt{\sum_i X_o(i)^2} \tag{18}$$

where, X_o is the original signal, and X' is the reconstructed signal.

The RMSEs of the three methods are demonstrated in Table 2. From these results of the simulation and calculation, we can easily draw the conclusions as follows. Firstly, direct Fourier method is unworkable for the near-field SAIR. With the imaging distance decreasing, its reconstruction effect is poorer. And its RMSE is the biggest one. Secondly, the modified Fourier method with quadratic phase-modified item has a better performance than the direct Fourier method, but still maintains unacceptable errors especially in extreme near-field

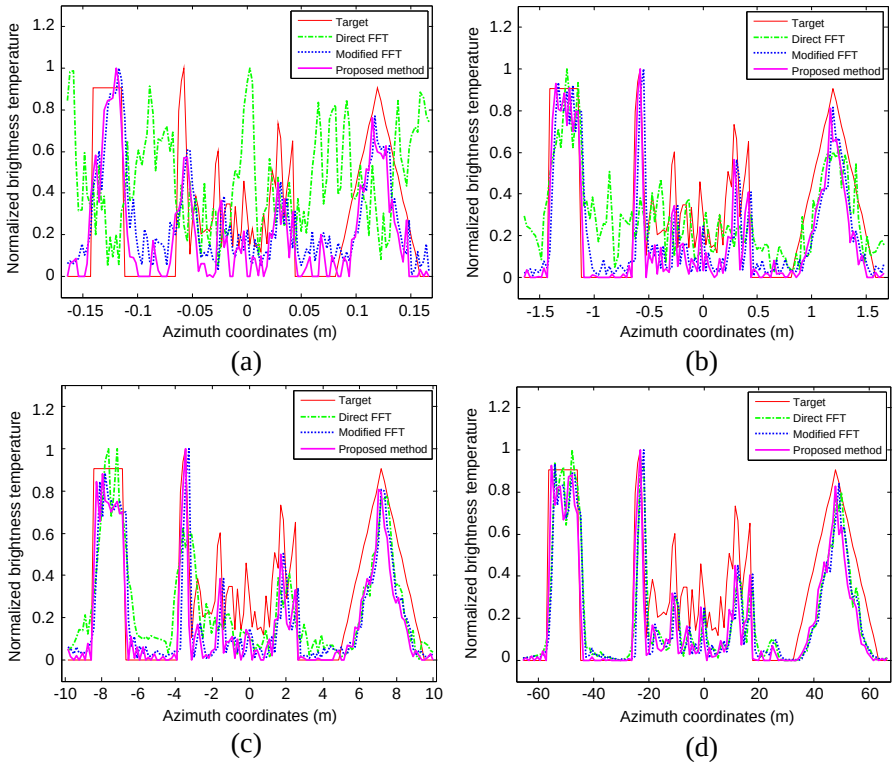

Figure 4. The simulation results of the 1-d extended source. The imaging distance of (a)–(d) is 1 m, 10 m, 60 m and 400 m respectively.

case. Thirdly, the accurate imaging method proposed in this paper is quite competent for SAIR imaging no matter in near-field or far-field case, and performs the best imaging effect among the three methods. Finally, with the imaging distance increasing, the reconstructed results of three methods are consistent with each other gradually.

Table 2. Comparison between FFTs and proposed imaging method.

Imaging distance (m)	**RMSE** Direct FFT	Modified FFT	Proposed method
1	0.3581	0.2133	0.1946
10	0.2473	0.2191	0.1892
60	0.2166	0.2052	0.1755
400	0.2129	0.2037	0.1735

4.3. Two-dimensional Simulation Experiments

For further demonstrating the effectiveness of the proposed imaging method, four groups of two-dimensional imaging simulation experiments are performed here. The target scene radiation intensity (brightness temperature) distribution is shown in Fig. 5, with its gray value as the radiation intensity of the discrete radiation sources, and the distance between the radiation sources is set as the system spatial resolution.

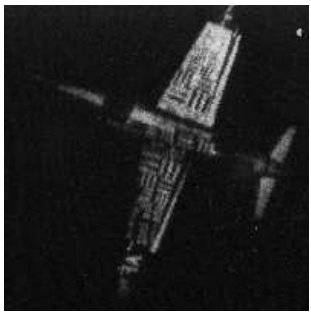

Figure 5. Brightness temperature distribution.

Due to the received signals obtained by integral in these simulation experiments, the calculation amount is very large, and its computational complexity is about $O(MKN^2)$, where M is the antenna array size, K the sampling signal length, and N the target scene size. For example, the size of target scene is a 100×100 gray image, received signal length 4096, "T" antenna array still 40×40, and the computing time of the visibility function on a personal computer with two 2.1-GHz AMD processors is about 30 minutes. If the target scene dimension enhances to 200×200, the computing time will increase to an unacceptable level (about 8 hours). So, the target scene is selected as 100×100 in this paper. It is worth noting that the large computing time is not affiliated to the proposed algorithm itself. Actually, the calculation of this proposed method only includes the calculations of matrixes $D1$ and $D2$ and solution of Eq. (16), and its algorithm complexity is $O(N^2)$. Due to the fact that the FGP is a fast method with the accelerated convergence rate, the real image reconstruction time takes only a few seconds.

The images are reconstructed by the direct Fourier method, modified Fourier method with phase-modified item, and the proposed imaging, respectively. The imaging distances are still set as in Table 1.

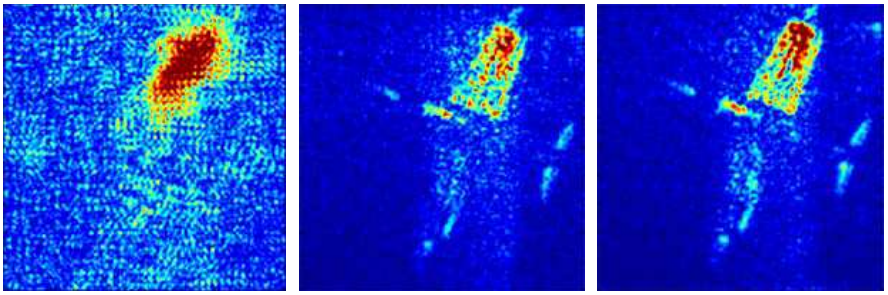

(a) (b) (c)

Figure 6. The images reconstructed by (a) direct Fourier method, (b) modified Fourier method, and (c) the proposed method. The imaging distance is 1 m.

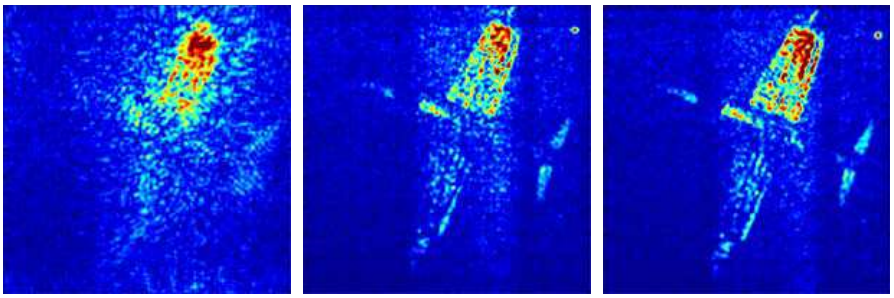

(a) (b) (c)

Figure 7. The images reconstructed by (a) direct Fourier method, (b) modified Fourier method, and (c) the proposed method. The imaging distance is 10 m.

The corresponding simulation results are shown in Figs. 6–9. It can be seen from the above simulation results that the direct Fourier method is only applicable to the far-field, that its reconstructed images are very blur in near-field, and that there is serious noise pollution near the target. The modified Fourier method with the phase-modified item can overcome these deficiencies to some extent, but the noise pollution near the target still exists. Clearly, the image reconstructed by the proposed accurate method is more accurate than the results of the Fourier methods. No matter in the near-field or far-field case, the low light noise pollution is eliminated better than the Fourier results.

In order to evaluate the accuracies of the three methods quantitatively, we define the structural similarity (SSIM) and the peak

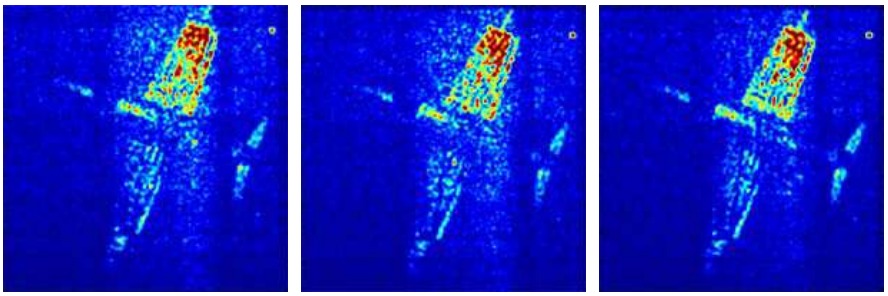

(a) (b) (c)

Figure 8. The images reconstructed by (a) direct Fourier method, (b) modified Fourier method, and (c) the proposed method. The imaging distance is 60 m.

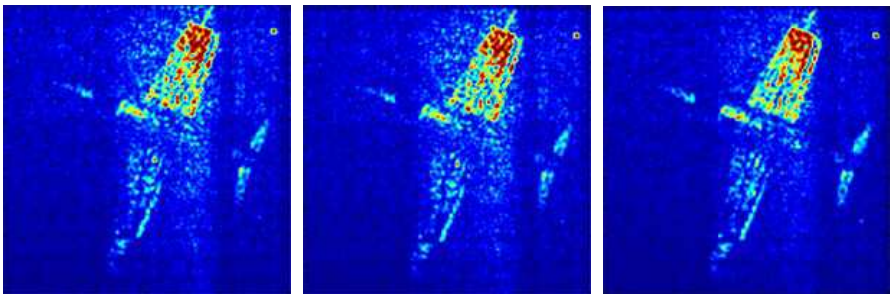

(a) (b) (c)

Figure 9. The images reconstructed by (a) direct Fourier method, (b) modified Fourier method, and (c) the proposed method. The imaging distance is 400 m.

signal-to-noise ratio (PSNR) as follows

$$\mathrm{SSIM}\left(\tilde{T},T_o\right)=\frac{\left(2\mu_{\tilde{T}}\mu_{T_o}+C_1\right)\left(\sigma_{\tilde{T}T_o}+C_2\right)}{\left(\mu_{\tilde{T}}^2+\mu_{T_o}^2+C_1\right)\left(\sigma_{\tilde{T}}^2+\sigma_{T_o}^2+C_2\right)} \tag{19}$$

$$\mathrm{PSNR}\left(\tilde{T},T_o\right)=10\log_{10}\frac{\max(T_o)^2}{\sum\limits_{0<i<M,0<j<N}\left[\tilde{T}(i,j)-T_o(i,j)\right]^2/M\times N} \tag{20}$$

where, $\tilde{T}$ is the reconstructed image, and T_o is the original one. $\mu_{\tilde{T}}$ and μ_{T_o} are the mean of image $\tilde{T}$ and T_o separately. $\sigma_{\tilde{T}}$ and σ_{T_o} are

Table 3. Comparison of objective data between FFTs and proposed method.

Imaging distance (m)	SSIM			PSNRs (dB)		
	Direct FFT	Modified FFT	Proposed method	Direct FFT	Modified FFT	Proposed method
1	0.5311	0.9194	0.9352	7.3859	15.7763	16.2033
10	0.8645	0.9271	0.9462	13.5708	16.1998	17.2529
60	0.9120	0.9171	0.9413	15.2268	15.5021	16.9121
400	0.9141	0.9243	0.9422	15.4031	16.0884	16.8785

the standard deviation of image $\tilde{T}$ and T_o, respectively. $\sigma_{\tilde{T}T_o}$ is the covariance of image $\tilde{T}$ and T_o. C_1 and C_2 are the smallest positive constants. $\max(T_o)$ denotes the max value of the original image T_o.

The SSIM and PSNRs of the aforementioned three methods are calculated as shown in Table 3. Clearly, the SSIM and PSNRs of the proposed accurate imaging method are both much better than the Fourier methods especially in the near-field case. And the differences between the proposed method and Fourier methods decrease with the imaging distance increasing as expected.

5. CONCLUSION

Because the Fourier imaging methods based on far-field approximation are invalid for the near-field SAIR, the near-field imaging method is an urgent problem to be solved. In this paper, we establish an accurate imaging algorithm based on the synthetic aperture imaging theory for near-field SAIR. For more accurately reconstructing the millimeter wave images, the quadratic phase item and antenna pattern are added to this imaging method, and the regularization is adopted to reconstruct the images. Finally, for verifying the validity of the proposed algorithm, the simulation experiments of one- and two-dimensional synthetic aperture imaging are performed respectively. The simulation results show that a more accurate brightness temperature image than the images obtained by traditional methods can be reconstructed by the proposed imaging algorithm. Besides, the proposed algorithm not only can be used for near-field imaging, but also is suitable for far-field imaging. We will further improve the coefficient matrixes ($D1$ and $D2$) to improve the efficiency and expand the application of this accurate imaging method.

ACKNOWLEDGMENT

The authors would like to thank the anonymous reviewer and editors for their helpful comments and suggestions. This work is supported by the National (Jiangsu) Natural Science Foundation of China under Grants 60901008 (BK2010490) and 61001010, National Ministry Foundation of China under Grants 51305050102.

REFERENCES

1. Appleby, R. and R. N. Anderton, "Millimeter-wave and submillimeter-wave imaging for security and surveillance," *Proceedings of the IEEE*, Vol. 95, No. 8, 1683–1690, Aug. 2007.
2. Yujiri, L., M. Shoucri, and P. Moffa, "Passive millimeter wave imaging," *IEEE Microwave Magazine*, Vol. 4, No. 3, 39–50, Sep. 2003.
3. Sheen, M. D., D. L. McMakin, and T. E. Hall, "Three-dimensional millimeter-wave imaging for concealed weapon detection," *IEEE Trans. Microwave Theory and Techniques*, Vol. 49, No. 9, 1581–1592, Sep. 2001.
4. Ruf, S. C., C. T. Swift, A. B. Tanner, and D. M. Le Vine, "Interferometric synthetic aperture microwave radiometry for the remote sensing of the Earth," *IEEE Trans. Geoscience and Remote Sensing*, Vol. 26, No. 5, 597–611, Sep. 1998.
5. Le Vine, M. D. and J. C. Good, "Aperture synthesis for microwave radiometers in space," NASA Tech. Memo., 85033, Goddard Space Flight Center, Greenbelt, MD, Aug. 1983.
6. Camps, A., J. Bara, I. C. Sanahuja, and F. Torres, "The processing of hexagonally sampled signals with standard rectangular techniques: Application to 2-D large aperture synthesis interferometric radiometers," *IEEE Trans. Geoscience and Remote Sensing*, Vol. 35, No. 1, 183–190, Jan. 1997.
7. Le Vine, D. M., M. Haken, and T. C. Swift, "Development of the synthetic aperture radiometer-ESTAR and the next generation," *IEEE International Geoscience and Remote Sensing Symposium*, Vol. 2, 1260–1263, 2004.
8. Kainulainen, J., K. Rautiainen, S. Tauriainen, T. Auer, J. Kettunen, and M. Hallikainen, "First 2-D interferometric radiometer imaging of the earth from an aircraft," *IEEE Geoscience and Remote Sensing Letters*, Vol. 4, No. 2, 241–245, Apr. 2007.

9. Martín-Neira, M. and J. M. Goutoule, "A two-dimensional aperture-synthesis radiometer for soil moisture and ocean salinity observations," *ESA Bull.*, No. 92, 95–104, Nov. 1997.
10. Silvestrin, P., M. Berger, Y. Kerr, and J. Font, "ESA's second earth explorer opportunity mission: The soil moisture and ocean salinity mission — SMOS," *IEEE Geoscience and Remote Sensing Newsletter*, Vol. 118, 11–14, Mar. 2001.
11. Kerr, Y. H., F. Cabot, P. Richaume, and J. Font, "Soil moisture and ocean salinity mission: First in-flight results," *SPIE Newsroom Remote Sensing*, Vol. 19, May 2010.
12. Jacobs, L. E. and O. Furxhi, "Performance modeling of a passive interferometric millimeter-wave sensor," *Proceedings of SPIE*, Vol. 7309, Apr. 2009.
13. Lucotte, B. M., B. Grafulla-Gonzalez, and R. A. Harvey, "Array rotation aperture synthesis for short range imaging at millimeter wavelengths," *Radio Science*, Vol. 44, 2009.
14. Su, K., W. Z. Liu, B. R. Barat, D. E. Gary, H. Z. Michalopoulou, and J. F. Federici, "Two-dimensional interferometric and synthetic aperture imaging with a hybrid terahertz/millimeter wave system," *Applied Optics*, Vol. 49, No. 19, E13–E19, Jul. 2010.
15. Zhang, C., J. Wu, H. Liu, and Y. J. Yan, "Imaging algorithm for synthetic aperture interferometric radiometer in near field," *Science China Technological Sciences*, Vol. 54, No. 8, 2224–2231, 2011.
16. Walsh, K. P., B. Schulkin, D. Gary, J. F. Federici, R. Barat, and D. Zimdars, "Terahertz near-field interferometric and synthetic aperture imaging," *Proceedings of SPIE*, Vol. 5411, 1–9, Sep. 2004.
17. Laursen, B. and N. Skou, "Synthetic aperture radiometry evaluated by a two-channel demonstration model," *IEEE Trans. Geoscience and Remote Sensing*, Vol. 36, No. 3, 822–832, May 1998.
18. Duffo, N., I. Corbella, F. Torres, A. Camps, and M. Vall-Llossera, "Advantages and drawbacks of near field characterization of large aperture synthesis radiometers," *8th Specialist Meeting on Microwave radiometry and Remote Sensing Applications*, University La Sapienza, Rome, Feb. 2004.
19. Tanner, B. A., H. B. Lambrigsten, M. T. Gaier, and F. Torres, "Near field characterization of the GeoSTAR demonstrator," *Proceedings of IEEE International Geoscience and Remote Sensing Symposium*, Denver, Co, USA, Jul. 2006.

20. Butora, R., M. Martín-Neira, and A. L. Rivada-Antich, "Fringe-washing function calibration in aperture synthesis microwave radiometry," *Radio Science*, Vol. 38, No. 2, 15.1–5, Apr. 2003.
21. Romberg, J., "Imaging via compressive sampling," *IEEE Signal Processing Magazine*, Vol. 25, No. 2, 14–20, Mar. 2008.
22. Li, S. Y., X. Zhou, B. Ren, H.-J. Sun, and X. Lv, "A compressive sensing approach for synthetic aperture imaging radiometers," *Rrogress In Electromagnetics Research*, Vol. 135, 583–599, 2013.
23. Wright, S. J., R. D. Nowak, and M. A. T. Figueiredo, "Sparse reconstruction by separable approximation," *IEEE Trans. Signal Processing*, Vol. 57, No. 7, 2479–2493, Jul. 2009.
24. Figueiredo, M. A. T., R. D. Nowak, and S. J. Wright, "Gradient projection for sparse reconstruction: Application to compressed sensing and other inverse problems," *IEEE Journal of Selected Topics in Signal Processing*, Vol. 1, No. 4, 586–597, Apr. 2007.
25. Hale, E. T., W. Yin, and Y. Zhang, "Fixed-point continuation for L_1 minimization: Methodology and convergence," *SIAM Journal on Optimization*, Vol. 19, No. 3, 1107–1130, 2008.
26. Beck, A. and M. Teboulle, "A fast iterative shrinkage-thresholding algorithm for linear inverse problems," *SIAM Journal on Imaging Sciences*, Vol. 2, No. 1, 183–202, Mar. 2009.